Progress In Electromagnetics Research B, Vol. 88, 97–118, 2020

Improved Semi-Analytical Magnetic Field Solution for High-Speed Permanent-Magnet Machines with Permeable Retaining Sleeve Including Diffusion Effect

Gabriel A. Mendonça[1, *], Thales A. C. Maia[2], and Braz J. Cardoso Filho[2]

Abstract—This work presents a novel semi-analytical model for magnetic field calculation in a high-speed surface-mounted permanent-magnet machine with conducting and permeable retaining sleeve. The retaining sleeve with conducting material and non-homogeneous permeability affects the machine electromagnetic performance by altering main flux inductance and developed torque profile. This performance deviation can be attributed to eddy-current reaction field and saturation, the latter occurring due to pole-to-pole leakage flux. Saturation is modeled with a space-varying relative permeability, expressed as a Fourier series. Eddy-currents are evaluated with an auxiliary winding, defined as a surface current density in the conducting region. The proposed method is based on well-established Maxwell-Fourier method. This permits other analysis, such as slotting effect through subdomain technique. The assumptions considered for the developed semi-analytical solution in two-dimensional problem are presented in depth and confronted with finite-element method results, confirming validity of proposed methodology.

1. INTRODUCTION

High-speed (HS) machines, as compared with conventional machines, provide higher power and torque density with improved overall system efficiency [1]. Due to these advantages, HS machines constitute a superior solution in several application areas, such as such as medical appliances, energy systems, and high-end machining tools [2, 3]. In such systems, the direct drive solution permits the elimination of mechanical transmission, thus reducing the drive system weight while increasing its reliability [4, 5]. However, in this operating range, there are few adequate machine topologies. The available literature shows a tendency to the use of permanent-magnet (PM) synchronous machines, solid rotor induction machines (IMs), and switched reluctance machines (SRMs). The PM synchronous machines have superior electromagnetic performance, with higher power density and efficiency [4, 6]. Compared with PM synchronous machines, solid rotor IMs, with a robust rotor structure, have lower maintenance requirements and field weakening capabilities at lower costs [3, 7]. SRMs are considered when cost and robustness are critical [8].

For HS machines, design and manufacturing are critical. To achieve safe operation at rated conditions, the evaluation of phenomena usually neglected in standard 50/60 Hz machines is required. The challenging aspect is primarily related to strong interaction among electromagnetic performance, mechanical integrity, and thermal behavior [1, 9]. This demands additional attention to topology and material selection in order to ensure strict constraints [10]. For the electromagnetic performance analysis, accurate modeling method is required to evaluate complex magnetic structures [11].

Numerical methods, e.g., finite-element methods (FEM), are a consolidated technique, widely used for its capability of modeling complex structures and non-ideal materials properties [12–14]. In

Received 19 May 2020, Accepted 2 August 2020, Scheduled 7 September 2020

* Corresponding author: Gabriel Alves Mendonça (gforti@gmail.com).

[1] Graduate Program in Electrical Engineering, Universidade Federal de Minas Gerais, Brazil. [2] Department of Electrical Engineering, Universidade Federal de Minas Gerais, Av. Antônio Carlos 6627, 31270-901, Belo Horizonte, MG, Brazil.

design stages of HS electrical machines, FEM can provide precise results in a multiphysics simulation environment, where the electromagnetic, mechanical and thermal constraints are evaluated [6]. Nonetheless, these are time-consuming and require large storage memory [15, 16]. Diversely, (semi-) analytical methods provide fast and accurate results on magnetic fields calculations, which are preferable characteristics for application in optimization routines [17, 18]. Two types of analytical methods are commonly used for design purpose: magnetic equivalent circuit (MEC) and Maxwell-Fourier (MF) methods [19–21]. The mesh based MEC methods can account for complex geometrical structures and saturation. However, MEC is less flexible than MF method, as it requires meshing, and does not consider eddy-current reaction fields properly [11, 19] The MF methods (e.g., multi-layer models, eigenvalue model and subdomain technique) provide satisfactory accuracy for complex structures with less computation time than FEM. The adoption of a hybrid method, with the combination of MEC and MF methods, is proposed to accommodate the advantages of each technique [22, 23]. These (semi-)analytical models are suitable for optimization in design early stages, where analytical calculations can be done in order to constrain the machine dimensions [1, 24, 25]. They also offer great insight into the modeled phenomena [15], providing closed-form solution with proper problem simplification [26, 27]. For more complex problems, i.e., eddy-current and saturation analysis, the semi-analytical model provides great post-processing capabilities, allowing fast results analysis in the entire evaluated region for each individual magnetic source [11].

The Maxwell-Fourier method is still of great interest, being studied and improved [20, 28, 29]. It can be adopted to evaluate magnetic field distribution in a wide range of machine topologies [30, 31]. However, the compromise between result accuracy and the adopted assumptions, which are used to limit model complexity, must be considered. These assumptions are related to geometry structure, material electromagnetic parameters, and magnetic source profile. Different techniques using geometry simplification are adopted to evaluate slotting effect, where slot opening is defined with radial sides and no tooth-tips [25, 32]. On the other hand, MF method can also evaluate realistic machine characteristics, such as asymmetric tooth-tips [33] and rotor eccentricities [34]. These capabilities help the proper analysis of cogging torque [35, 36]. Furthermore, recent improvements are proposed to calculate magnetic field distribution in the ferromagnetic material of slotted geometries, viz., the convolution theorem [37] and Dubas' superposition technique [28, 38]. For source terms, the assumption of balanced stator currents under steady-state operation are used to evaluate eddy-current reaction field. The balanced condition is not method-wise but needs to manipulate the diffusion equation into the Helmholtz equation form [11, 39, 40].

There are few works that properly model the retaining sleeve (RS) material properties. RS is adopted in HS PM machines to ensure magnet mechanical integrity [9] and usually is made of non-magnetic material that may be conductive or non-conductive [41]. For conduction material, such as stainless steel or Incomel 718, eddy-current reaction fields affect rotor losses [15, 42–44] and machine produced torque [45–47]. Also, there are works evaluating the advantages of using permeable RS, which includes reduced PM usage and increased inductance [45, 48, 49]. These permeable RSs present nonlinear $B(H)$ characteristics and affects the machine performance [50, 51].

In this paper, a novel formulation based on MF method is developed to consider nonhomogeneous permeability. The space-varying magnetic permeability, defined through Fourier series [51], is extended to account for slotting effect using subdomain method. In comparison with other methods to evaluate slotting effect, this provides the most accurate results [35, 52]. For the evaluation of eddy-current reaction fields, a surface current density is defined in the RS region. This auxiliary winding, as discussed in [53], was first proposed for a PM machine whose characteristics permitted the skin effect to be disregarded. In the present work, the authors evaluate the skin effect by reexamining the auxiliary winding parameters. With this definition, the method can analyze a high-speed permanent-magnet machine under transient and unbalanced conditions. Finally, this paper presents a thorough discussion of the assumptions made, as they are strong and need to be evaluated carefully. The validation of the proposed model is carried out based on a two-pole surface-mounted PM generator prototype with stainless steel RS. The derived model is evaluated for different operating conditions, and the results are compared with those obtained from FEM. For the latter, this work uses the program Finite Element Method Magnetics (FEMM), a free finite-element analysis software package [14].

2. PROBLEM DESCRIPTION AND EVALUATED PROTOTYPE

The (semi-)analytical method accuracy is related to the assumptions, such as the presence of slotting effect, material parameters, number of evaluated regions (or concentric layers), magnetization pattern, and type of excitation current [15].

This work is intended to reevaluate such commonly used approximations, and it is based on the analysis of an HS generator prototype, which is part of a micro-compressed air energy storage (micro-CAES) system. This system was built from a commercial automotive turbocharger, which provides a low cost solution to support small renewable energy plants. The high-speed generator, compressor, and turbine were mounted on a single common shaft, as illustrated in the three-dimensional model in Fig. 1(a). The assembled prototype with interior generator is pictured in Fig. 1(b). Some aspects of this machine were discussed in previous work. For the micro-CAES system, an experimental study on its performance is presented in [54], which evaluates overall system efficiency. Moreover, the concepts and issues related to the electromechanical design are further discussed in [10, 55], where HS generator materials are analyzed according to its effect on the operational losses.

(a) (b)

Figure 1. High-speed micro-CAES system: (a) three-dimensional model; and (b) assembled micro-CAES prototype [10].

The constructed electric machine consists of a two-pole high-speed surface-mounted PM generator. The rotor was manufactured with NdFeB-N48H ring shape magnet with parallel magnetization. To acquire proper PM banding requirement, a stainless steel AISI 310 sleeve was adopted. The assemble prototype is illustrated in Fig. 2, and the machine characteristics are presented in Table 1.

The design of HS machine is critical, demanding attention to machine topology, material selection, manufacturing procedure, and many other critical aspects. For the studied HS generator to attend the remarkably high balancing grade [9], magnet and RS were machined to fit geometric tolerances. This

Table 1. Prototype PM machine characteristics.

Parameters	**Value**
Induced voltage	220 V_{rms}
Rated speed	70,000 rpm
Rated current	9.2 A_{rms}
Rated power	3.5 kW
PM material	NdFeB-N48H
RS material	Stainless steel AISI 310
Core material	*Aperam* Steel (0.35 mm)
Copper wire gauge	28 AWG

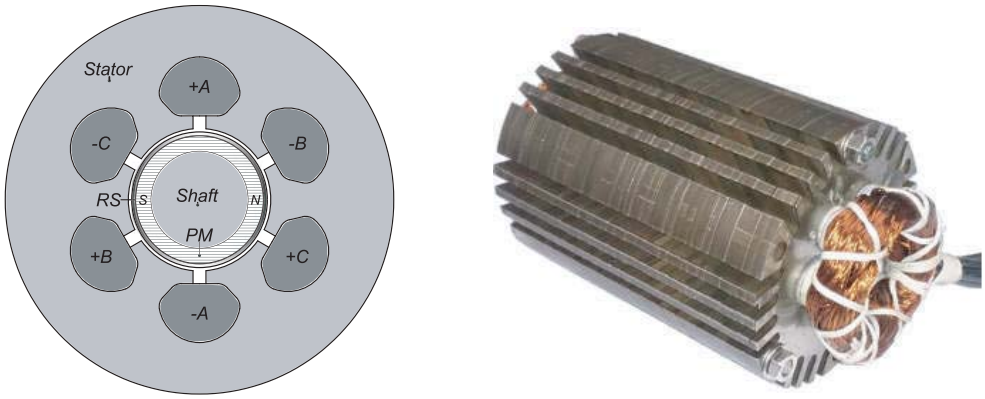

(a) (b)

Figure 2. PM generator: (a) schematic view; and (b) assembled prototype stator [51].

procedure caused considerable reduction in PM residual flux density [55]. The RS lost its austenitic properties, exhibiting increased permeability.

As evaluated in [51], the permeable RS causes pole-to-pole leakage flux and a resulting local saturation phenomenon. With a higher permeability and established preferable magnetic path, the machine inductance is increased. Moreover, oscillating torque profile is changed due to the greater spatial harmonic of airgap flux density [56].

Other works propose alternative solutions to obtain a permeable RS, such as cold-worked stainless steel [50] and RS made of permalloy [49]. This is justified for its advantages, including the use of thinner PM with unchanged back-EMF and mean torque. Therefore, the proposed method is developed with the objective of improving the MF method capabilities, evaluating non-homogeneous magnetic parameter in a conducting region.

3. GEOMETRY AND MATHEMATICAL FORMULATION

3.1. Model Assumptions

The MF method is based on the formal resolution of Maxwell's equations in different electric machine regions, defined as coaxial cylinders. The solution for governing equations in each region is obtained using the method of separation of variables. For the periodic problem, the solution is expressed as a Fourier series [57].

The proposed model is developed based on this well-established MF solution to magnetic field distribution in surface-mounted PM machine. The adopted semi-analytical model is formulated with the following assumptions:

- the stator and rotor iron are infinitely permeable;
- the end-effects are negligible (i.e., magnetic variables do not vary along the machine axial length);
- slot with simple geometry (no tooth-tip);
- the electrical conductivity of PM is assumed null, and
- the magnets have linear demagnetization characteristic.

Therefore, the two-dimensional analytical problem is evaluated in the machine geometry, illustrated in Fig. 3.

The slotting effect is evaluated through subdomain method as developed in [25, 58, 59] and improved in [60]. With approximation of infinitely permeable stator iron, it is solved with homogeneous Neumann boundary condition [28]. In surface-mounted PM machines, the simplified model, which neglects stator tooth-tips, provides similar results to those taking the tooth-tips into account [35]. All magnetic quantities are calculated in the stator angular coordinate, φ_s, which is defined from stator phase a magnetic axis in the *abc*-reference system. Alternatively, the rotor angular coordinate, φ_r, is measured

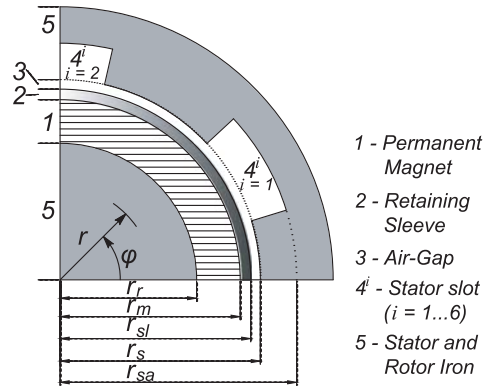

Figure 3. A quarter cross section model of PM synchronous machine for analytical calculation.

from the PM magnetic axis and is displaced from the stator reference frame by the rotor angular position, θ, that is

$$\varphi_s = \varphi_r + \theta. \tag{1}$$

The saturation in the RS region is a result of pole-to-pole leakage flux, and the subsequent relative permeability will vary along the RS circumferential length. Therefore, for a considerably thin RS, relative permeability is invariable in the radial direction and is periodical in the circumferential direction with a fundamental space period equal to π/p, where p is the number of pole pairs. Considering the asymmetries in the magnetic quantities related to the subdomain method, the relative permeability distribution is defined generically in terms of a Fourier series as

$$\mu_r(\varphi_s) = \sum_{m=0,1,2,3,\ldots}^{\infty} \left[\hat{\mu}_{(c)r,m}\cos(2pm\varphi_s) + \hat{\mu}_{(s)r,m}\sin(2pm\varphi_s)\right], \tag{2}$$

where $\mu_r(\varphi)$ is the space-varying relative permeability, defined as a function of mechanical angle, m the space harmonic, $\hat{\mu}_{(c)r,m}$ the Fourier cosine coefficient, and $\hat{\mu}_{(s)r,m}$ the Fourier sine coefficient. The Fourier coefficients are calculated using iterative methods to account for the nonlinear magnetic material, as will be discussed later on. It is interesting to note that, for a homogeneous permeability, only the average value exists, i.e., $\mu_r(\varphi_s) = \hat{\mu}_{(c)r,0}$.

An important approximation needed to the novel method is that the relative permeability variation along the RS circumferential direction is small. Assuming the Coulomb gauge, i.e., $\nabla \cdot \mathbf{A} = 0$, the magnetic vector potential formulation can be approximated as

$$\nabla \times \left(\frac{1}{\mu(\varphi_s)}\nabla \times \mathbf{A}\right) \approx -\frac{1}{\mu(\varphi_s)}\nabla^2\mathbf{A}. \tag{3}$$

3.2. Poisson's Equation General Solution and Boundary Conditions

The two-dimensional semi-analytical problem is formulated adopting the magnetic vector potential and listed assumptions. The general partial-differential equation from the Maxwell's equation and constitutive relations can be expressed as

$$-\nabla^2\mathbf{A} + \mu\sigma\frac{\partial \mathbf{A}}{\partial t} = \mu\mathbf{J}_s + \ \nabla \times \mathbf{B}_{rem}, \tag{4}$$

where $\mathbf{A}$ is the magnetic vector potential, $\mathbf{J}_s$ the stator current density, $\mathbf{B}_{rem}$ the remanent magnetization of the permanent magnets, μ the permeability, and σ the conductivity. This equation, which is simplified to consider only z-axis component of vector potential, A_z, is evaluated for each region and solved using separation of variables. The general solution to Poisson's equation is determined for periodic regions i.e., PM, RS and airgap, and can be expressed as

$$A_z^{(v)}(r,\varphi_s) = \sum_{k=1,3,5\ldots}^{\infty} \left(\hat{A}^{(v)}_{(s)z,k}(r)\sin(kp\varphi_s) + \hat{A}^{(v)}_{(c)z,k}(r)\cos(kp\varphi_s)\right), \tag{5a}$$

with

$$\hat{A}^{(v)}_{(s)z,k}(r) = \left(C^{(v)}_k \left(\frac{r}{r_v}\right)^{-kp} + D^{(v)}_k \left(\frac{r}{r_v}\right)^{kp} + \hat{A}^{(v)}_{(s)part,z,k} r \right), \tag{5b}$$

$$\hat{A}^{(v)}_{(c)z,k}(r) = \left(E^{(v)}_k \left(\frac{r}{r_v}\right)^{-kp} + F^{(v)}_k \left(\frac{r}{r_v}\right)^{kp} + \hat{A}^{(v)}_{(c)part,z,k} r \right), \tag{5c}$$

where the regions are defined according to Fig. 3, with $v = 1, 2, 3$, and 4^i for PM, RS, airgap, and i-th stator slot, respectively. The magnetic vector potential in region v, $A^{(v)}_z$, is described through a series of space harmonics k. The radius at the interface of regions v and $v+1$, r_v, is used to normalize the radius r. The sine and cosine Fourier coefficients, $\hat{A}^{(v)}_{(s)z,k}(r)$ and $\hat{A}^{(v)}_{(c)z,k}(r)$ respectively, are subject of several studies, and the results depend on problem assumptions, such as the magnetization profile for PM region (e.g., parallel, radial, Halbach, etc.). The particular solutions, $\hat{A}^{(v)}_{(s)part,z,k}$ and $\hat{A}^{(v)}_{(c)part,z,k}$, are needed to characterize the magnetic field in regions with source terms. The integration constants are $C^{(v)}_k$, $D^{(v)}_k$, $E^{(v)}_k$, and $F^{(v)}_k$.

For regions where no source terms are defined, such as the air-gap and RS, the Poisson's Equation (4) is simplified to the corresponding Laplace's equation. The solution to the Laplace's equation is obtained from Eq. (5) disregarding the particular solution for the sine and cosine Fourier coefficients, i.e., $\hat{A}^{(v)}_{(s)part,z,k} = 0$ and $\hat{A}^{(v)}_{(c)part,z,k} = 0$, respectively.

In the present investigation, where the focus is to characterize saturation in the RS region, the Fourier coefficients can be omitted without losing generality. For further information, an overview on Maxwell-Fourier methods is provided in [11]. More detailed discussion on the solution for PM with different magnetization profiles is given in [58, 61]. For the evaluation of more realistic permanent-magnet structure, such as segmented magnet and separated magnet bars, the Amperian equivalent model is adopted [62].

The Poisson's solution for non-periodic regions, i.e., stator slots, is expressed as

$$A^{(4i)}_z(r, \varphi_s) = \hat{A}^{(4i)}_{z,0}(r) + \sum_n \hat{A}^{(4i)}_{z,n}(r) \cos\left(E_n \left(\varphi_s - \Phi_i + \frac{b_{sa}}{2} \right) \right), \tag{6a}$$

with the Fourier constants, $A^{(4i)}_{z,0}$ and $A^{(4i)}_{z,n}$, defined as

$$A^{(4i)}_{z,0} = \frac{1}{4}\mu_0 J_{i0} \left(2r^2_{sa} ln(r) - r^2 \right) + Q_{4i}, \tag{6b}$$

$$A^{(4i)}_{z,n} = r_s \left(\left(\frac{r}{r_{sa}}\right)^{2E_n} + 1 \right) \left(\frac{r}{r_s}\right)^{-E_n} C^{(4i)}_n + \mu_0 \frac{J_{in}}{(E^2_n - 4)} \left(r^2 - \frac{2}{E_n} r^2_{sa} \left(\frac{r}{r_{sa}}\right)^{E_n} \right), \tag{6c}$$

where Φ_i is the i-th slot position, b_{sa} the slot width angle, and $E_n = n\pi/b_{sa}$. The integration constants are $C^{(4i)}_n$ and Q_{4i}. The solution is determined depending on winding layout, i.e., single-layer or double-layer with overlapping or non-overlapping configurations. These different configurations are characterized with the terms J_{i0} and J_{in}. Further discussion on subdomain method for different winding layouts and machine topologies is found in [21, 31, 59].

The integration constants in the Fourier series are determined by the boundary conditions between the domains v and $v+1$, that is

$$H^{(v+1)}_\varphi(r_v, \varphi_s) - H^{(v)}_\varphi(r_v, \varphi_s) = K^{(v)}_z(\varphi_s), \tag{7}$$

$$B^{(v+1)}_r(r_v, \varphi_s) - B^{(v)}_r(r_v, \varphi_s) = 0 \tag{8}$$

where r_v is the radius at the interface, and $K^{(v)}_z$ is a surface current density. Expressions for the tangential field intensity, H_φ, and normal flux density, B_r, are derived from magnetic potential vector definition, $\mathbf{B} = \nabla \times \mathbf{A}$, and magnetic constitutive relation, $\mathbf{B} = \mu\mathbf{H} + \mathbf{B}_{rem}$. Therefore, from the relative permeability distribution, Eq. (2), the present formulation is based on the reevaluation of tangential

boundary condition. Therefore, for each of the RS interfaces, i.e., with airgap and PM, Eq. (7) is expressed as

$$\frac{B_{\varphi}^{(2)}\left(r_{sl},\varphi_s\right)}{\mu_r\left(\varphi_s\right)\mu_0} = \frac{B_{\varphi}^{(3)}\left(r_{sl},\varphi_s\right)}{\mu_0}, \tag{9}$$

$$\frac{B_{\varphi}^{(2)}\left(r_{m},\varphi_s\right)}{\mu_r\left(\varphi_s\right)\mu_0} = \frac{B_{\varphi}^{(1)}\left(r_{m},\varphi_s\right) - B_{rem\prime\varphi}}{\mu_{rec}\mu_0}, \tag{10}$$

where μ_{rec} is the relative recoil permeability, and $B_{rem\prime\varphi}$ is the circumferential component of the PM remanent magnetization. This circumferential component can be expressed in terms of a Fourier series, written in the stator reference frame as

$$B_{rem,\varphi} = \sum_{k=1,3,5,\ldots}^{\infty}\left[\hat{B}_{(s)rem,\varphi,k}\sin\left(kp\varphi_s\right) + \hat{B}_{(c)rem,\varphi,k}\cos\left(kp\varphi_s\right)\right], \tag{11}$$

where $\hat{B}_{(s)rem,\varphi,k}$ and $\hat{B}_{(c)rem,\varphi,k}$ are the sine and cosine Fourier coefficients, respectively. The magnetization pattern is characterized using these terms.

Using the relative permeability defined from Eq. (2), the boundary condition (9) can be rewritten as

$$\begin{aligned}
&\sum_{k=1,2,3,\ldots}^{\infty}\left[\hat{B}_{(s)\varphi,k}^{(2)}\left(r_{sl}\right)\sin\left(kp\varphi_s\right) + \hat{B}_{(c)\varphi,k}^{(2)}\left(r_{sl}\right)\cos\left(kp\varphi_s\right)\right] \\
&= \sum_{m=0,1,2,3,\ldots}^{\infty}\left[\hat{\mu}_{(c)r,m}\cos\left(2mp\varphi_s\right) + \hat{\mu}_{(s)r,m}\sin\left(2mp\varphi_s\right)\right] \\
&\quad\times\sum_{n=1,2,3,\ldots}^{\infty}\left[\hat{B}_{(s)\varphi,k}^{(3)}\left(r_{sl}\right)\sin\left(np\varphi_s\right) + \hat{B}_{(c)\varphi,k}^{(3)}\left(r_{sl}\right)\cos\left(np\varphi_s\right)\right],
\end{aligned} \tag{12}$$

where the Fourier summation indexes are defined with different variables, k, m, and n, for generalization purposes. As discussed in [51], the Fourier constants are determined observing the orthogonality of the sine and cosine functions, that is

$$\hat{B}_{(s)\varphi,k}^{(2)}\left(r_{sl}\right) = \frac{1}{\pi}\int_0^{2\pi} f\left(\varphi_s\right)\sin\left(kp\varphi_s\right)d\varphi \tag{13}$$

and

$$\hat{B}_{(c)\varphi,k}^{(2)}\left(r_{sl}\right) = \frac{1}{\pi}\int_0^{2\pi} f\left(\varphi_s\right)\cos\left(kp\varphi_s\right)d\varphi, \tag{14}$$

where $f(\varphi_s)$ is the right-hand side of the Eq. (12). Rearranging Eqs. (13) and (14) yields the following relations for the Fourier coefficients

$$\begin{aligned}
\hat{B}_{(s)\varphi,k}^{(2)}\left(r_{sl}\right) &= \sum_{m=0,1,2,3,\ldots}^{\infty}\sum_{n=1,3,5\ldots}^{\infty}\frac{\hat{\mu}_{(c)r,m}\hat{B}_{(s)\varphi,n}^{(3)}\left(r_{sl}\right)}{\pi}\int_0^{2\pi}\cos\left(2mp\varphi_s\right)\sin\left(np\varphi_s\right)\sin\left(kp\varphi_s\right)d\varphi \\
&+ \sum_{m=0,1,2,3,\ldots}^{\infty}\sum_{n=1,3,5\ldots}^{\infty}\frac{\hat{\mu}_{(c)r,m}\hat{B}_{(c)\varphi,n}^{(3)}\left(r_{sl}\right)}{\pi}\int_0^{2\pi}\cos\left(2mp\varphi_s\right)\cos\left(np\varphi_s\right)\sin\left(kp\varphi_s\right)d\varphi \\
&+ \sum_{m=0,1,2,3,\ldots}^{\infty}\sum_{n=1,3,5\ldots}^{\infty}\frac{\hat{\mu}_{(s)r,m}\hat{B}_{(s)\varphi,n}^{(3)}\left(r_{sl}\right)}{\pi}\int_0^{2\pi}\sin\left(2mp\varphi_s\right)\sin\left(np\varphi_s\right)\sin\left(kp\varphi_s\right)d\varphi \\
&+ \sum_{m=0,1,2,3,\ldots}^{\infty}\sum_{n=1,3,5\ldots}^{\infty}\frac{\hat{\mu}_{(s)r,m}\hat{B}_{(c)\varphi,n}^{(3)}\left(r_{sl}\right)}{\pi}\int_0^{2\pi}\sin\left(2mp\varphi_s\right)\cos\left(np\varphi_s\right)\sin\left(kp\varphi_s\right)d\varphi
\end{aligned} \tag{15}$$

and

$$\hat{B}^{(2)}_{(c)\varphi,k}(r_{sl}) = \sum_{m=0,1,2,3,\ldots}^{\infty}\sum_{n=1,3,5\ldots}^{\infty}\frac{\hat{\mu}_{(c)r,m}\hat{B}^{(3)}_{(s)\varphi,n}(r_{sl})}{\pi}\int_0^{2\pi}\cos(2mp\varphi_s)\sin(np\varphi_s)\cos(kp\varphi_s)\,d\varphi$$
$$+\sum_{m=0,1,2,3,\ldots}^{\infty}\sum_{n=1,3,5\ldots}^{\infty}\frac{\hat{\mu}_{(c)r,m}\hat{B}^{(3)}_{(c)\varphi,n}(r_{sl})}{\pi}\int_0^{2\pi}\cos(2mp\varphi_s)\cos(np\varphi_s)\cos(kp\varphi_s)\,d\varphi$$
$$+\sum_{m=0,1,2,3,\ldots}^{\infty}\sum_{n=1,3,5\ldots}^{\infty}\frac{\hat{\mu}_{(s)r,m}\hat{B}^{(3)}_{(s)\varphi,n}(r_{sl})}{\pi}\int_0^{2\pi}\sin(2mp\varphi_s)\sin(np\varphi_s)\cos(kp\varphi_s)\,d\varphi$$
$$+\sum_{m=0,1,2,3,\ldots}^{\infty}\sum_{n=1,3,5\ldots}^{\infty}\frac{\hat{\mu}_{(s)r,m}\hat{B}^{(3)}_{(c)\varphi,n}(r_{sl})}{\pi}\int_0^{2\pi}\sin(2mp\varphi_s)\cos(np\varphi_s)\cos(kp\varphi_s)\,d\varphi, \quad (16)$$

where the space harmonic index k can be thought as a reference index. The integration on the right-hand side of Eqs. (15) and (16) will be different from zero only for specific values of k, m, and n. Summarizing the results, Table 2 presents the index relations which results in non-zero integration values in Eq (15), and Table 3 is for relations in Eq. (16).

Table 2. Space harmonic index relations for non-zero integral solutions of sine Fourier coefficients.

Integral	Index Relation	Integral Result
$\int_0^{2\pi}\cos(2mp\varphi_s)\sin(np\varphi_s)\sin(kp\varphi_s)\,d\varphi$	$n=k-2m$ $n=k+2m$ $n=2m-k$	$\frac{\pi}{2}$ $\frac{\pi}{2}$ $-\frac{\pi}{2}$
$\int_0^{2\pi}\cos(2mp\varphi_s)\cos(np\varphi_s)\sin(kp\varphi_s)\,d\varphi$	$\forall\ k,n,m$	0
$\int_0^{2\pi}\sin(2mp\varphi_s)\sin(np\varphi_s)\sin(kp\varphi_s)\,d\varphi$	$\forall\ k,n,m$	0
$\int_0^{2\pi}\sin(2mp\varphi_s)\cos(np\varphi_s)\sin(kp\varphi_s)\,d\varphi$	$n=k-2m$ $n=k+2m$ $n=2m-k$	$\frac{\pi}{2}$ $-\frac{\pi}{2}$ $\frac{\pi}{2}$

It is important to note that from the results in Tables 2 and 3, if the problem assumes homogeneous and constant RS relative permeability, i.e., for $m=0$, the solution is determined from interaction of magnetic fields with the same space harmonic order, that is $n=k$. In such a case, the presented formulation simplifies to the established MF solution. Additionally, the linear equations from the index relations are summed according to the evaluated relative permeability frequency content. Therefore, from these observations and the results afore presented, Eqs. (15) and (16) are solved to

$$\hat{B}^{(2)}_{(s)\varphi,k}(r_{sl}) = \sum_{m=0,1,2,3,\ldots}^{\infty}\left[\frac{\hat{\mu}_{(c)r,m}}{2}\left(\hat{B}^{(3)}_{(s)\varphi,k-2m}(r_{sl})+\hat{B}^{(3)}_{(s)\varphi,k+2m}(r_{sl})-\hat{B}^{(3)}_{(s)\varphi,2m-k}(r_{sl})\right)\right.$$
$$\left.+\frac{\hat{\mu}_{(s)r,m}}{2}\left(\hat{B}^{(3)}_{(c)\varphi,k-2m}(r_{sl})-\hat{B}^{(3)}_{(c)\varphi,k+2m}(r_{sl})+\hat{B}^{(3)}_{(c)\varphi,2m-k}(r_{sl})\right)\right] \quad (17)$$

and

$$\hat{B}^{(2)}_{(c)\varphi,k}(r_{sl}) = \sum_{m=0,1,2,3,\ldots}^{\infty}\left[\frac{\hat{\mu}_{(c)r,m}}{2}\left(\hat{B}^{(3)}_{(c)\varphi,k-2m}(r_{sl})+\hat{B}^{(3)}_{(c)\varphi,k+2m}(r_{sl})+\hat{B}^{(3)}_{(c)\varphi,2m-k}(r_{sl})\right)\right.$$
$$\left.+\frac{\hat{\mu}_{(s)r,m}}{2}\left(-\hat{B}^{(3)}_{(s)\varphi,k-2m}(r_{sl})+\hat{B}^{(3)}_{(s)\varphi,k+2m}(r_{sl})+\hat{B}^{(3)}_{(s)\varphi,2m-k}(r_{sl})\right)\right]. \quad (18)$$

Table 3. Space harmonic index relations for non-zero integral solutions of cosine Fourier coefficients.

Integral	Index Relation	Integral Result
$\int_0^{2\pi} \cos(2mp\varphi_s) \sin(np\varphi_s) \cos(kp\varphi_s)\, d\varphi$	$\forall\ k, n, m$	0
$\int_0^{2\pi} \cos(2mp\varphi_s) \cos(np\varphi_s) \cos(kp\varphi_s)\, d\varphi$	$n = k - 2m$ $n = k + 2m$ $n = 2m - k$	$\frac{\pi}{2}$ $\frac{\pi}{2}$ $\frac{\pi}{2}$
$\int_0^{2\pi} \sin(2mp\varphi_s) \sin(np\varphi_s) \cos(kp\varphi_s)\, d\varphi$	$n = k - 2m$ $n = k + 2m$ $n = 2m - k$	$-\frac{\pi}{2}$ $\frac{\pi}{2}$ $\frac{\pi}{2}$
$\int_0^{2\pi} \sin(2mp\varphi_s) \cos(np\varphi_s) \cos(kp\varphi_s)\, d\varphi$	$\forall\ k, n, m$	0

The same reasoning is used for the boundary condition between the PM and the RS, as defined in Eq. (10), and tangential component of the remanent magnetization from Eq. (11), giving the following relations

$$\begin{aligned}\hat{B}^{(2)}_{(s)\varphi,k}(r_m) \;=\; \sum_{m=0,1,3,5,\ldots}^{\infty} \Bigg[& \frac{\hat{\mu}_{(c)r,m}}{2\mu_{rec}} \Big(\hat{B}^{(1)}_{(s)\varphi,k-2m}(r_m) + \hat{B}^{(1)}_{(s)\varphi,k+2m}(r_m) - \hat{B}^{(1)}_{(s)\varphi,2m-k}(r_m) \\ & - \hat{B}_{(s)rem,\varphi,k-2m} - \hat{B}_{(s)rem,\varphi,k+2m} + \hat{B}_{(s)rem,\varphi,2m-k} \Big) \\ & + \frac{\hat{\mu}_{(s)r,m}}{2\mu_{rec}} \Big(\hat{B}^{(1)}_{(c)\varphi,k-2m}(r_m) - \hat{B}^{(1)}_{(c)\varphi,k+2m}(r_m) + \hat{B}^{(1)}_{(c)\varphi,2m-k}(r_m) \\ & - \hat{B}_{(c)rem,\varphi,k-2m} + \hat{B}_{(c)rem,\varphi,k+2m} - \hat{B}_{(c)rem,\varphi,2m-k} \Big) \Bigg] \end{aligned} \tag{19}$$

and

$$\begin{aligned}\hat{B}^{(2)}_{(c)\varphi,k}(r_m) \;=\; \sum_{m=0,1,3,5,\ldots}^{\infty} \Bigg[& \frac{\hat{\mu}_{(c)r,m}}{2\mu_{rec}} \Big(\hat{B}^{(1)}_{(c)\varphi,k-2m}(r_m) + \hat{B}^{(1)}_{(c)\varphi,k+2m}(r_m) + \hat{B}^{(1)}_{(c)\varphi,2m-k}(r_m) \\ & - \hat{B}_{(c)rem,\varphi,k-2m} - \hat{B}_{(c)rem,\varphi,k+2m} - \hat{B}_{(c)rem,\varphi,2m-k} \Big) \\ & + \frac{\hat{\mu}_{(s)r,m}}{2\mu_{rec}} \Big(- \hat{B}^{(1)}_{(s)\varphi,k-2m}(r_m) + \hat{B}^{(1)}_{(s)\varphi,k+2m}(r_m) + \hat{B}^{(1)}_{(s)\varphi,2m-k}(r_m) \\ & + \hat{B}_{(s)rem,\varphi,k-2m} - \hat{B}_{(s)rem,\varphi,k+2m} - \hat{B}_{(s)rem,\varphi,2m-k} \Big) \Bigg]. \end{aligned} \tag{20}$$

From Eqs. (17) and (18), it can be verified that the Fourier coefficients of the magnetic flux density in the non-homogeneous region, $v = 2$, are related to those of different space harmonic orders of the surrounding regions, i.e., $v = 1$ and 3. Also, introducing the space-varying permeability leads to mutual dependence of cosine and sine Fourier coefficients. For example, the cosine Fourier coefficient $\hat{B}^{(2)}_{(c)\varphi,k}$ is expressed in terms of cosine Fourier coefficients, $\hat{B}^{(3)}_{(c)\varphi,k-2m}$, $\hat{B}^{(3)}_{(c)\varphi,k+2m}$ and $\hat{B}^{(3)}_{(c)\varphi,2m-k}$, and the sine coefficients, $\hat{B}^{(3)}_{(s)\varphi,k-2m}$, $\hat{B}^{(3)}_{(s)\varphi,k+2m}$ and $\hat{B}^{(3)}_{(s)\varphi,2m-k}$, which are defined in the space harmonic orders of $(k-2m)$, $(k+2m)$, and $(2m-k)$. The index m is the space harmonic order of the relative permeability Fourier series. Finally, considering $\{\forall k \in \mathbf{N},\ k \leq K_{\max}\}$, where $K_{\max}$ is the maximum evaluated space harmonic order, $(k-2m)$, $(k+2m)$, and $(2m-k)$ are also limited to the interval $[0, K_{\max}]$.

3.3. Nonlinear Solution Algorithm

The saturation of the permeable RS is a consequence of pole-to-pole leakage flux. With the considerably thin RS, the region relative permeability is assumed to vary primarily along the RS. Furthermore, the periodical behavior of this permeability permits the adoption of a mathematical definition in terms of a Fourier series, as presented in Section 3.1. The RS saturation level is evaluated by an iterative method, with the overall diagram illustrated in Fig. 4(a). The diagram pictured in Fig. 4(b) presents the detailed method to calculate the new relative permeability profile at each iteration.

Starting with an initial permeability profile, $\mu_{r,test}$, the magnetic flux density is calculated in the RS mean radius using the described MF method. With the absolute value of this flux density, $|B(r_{mean}, \varphi)|$ and the material $B(H)$ curve, the relative permeability profile along the RS circumferential direction is obtained, as illustrated in Fig. 4(b). This new permeability value, $\mu_{r,new}$, is compared with the previous one, $\mu_{r,test}$ using mean absolute percentage error (MAPE). The convergence is evaluated, with ξ specified as the maximum permitted error.

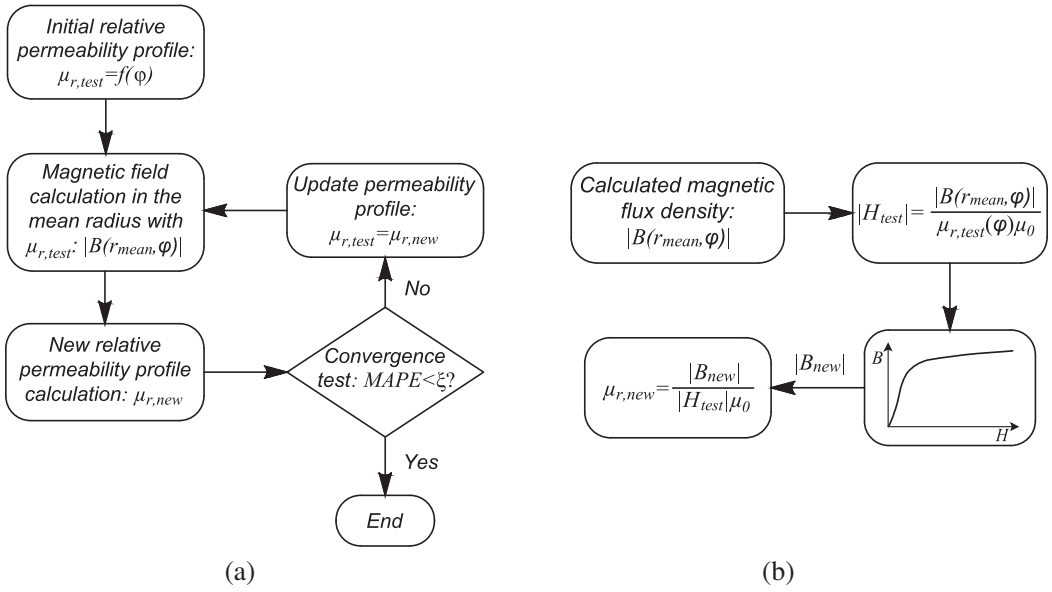

Figure 4. Diagram for estimation of the saturation level: (a) overall iterative flowchart; and (b) new relative permeability profile calculation, $\mu_{r,new}$, flowchart.

For the new relative permeability profile calculation, $\mu_{r,new}$, the $B(H)$ curve is used to obtain a new magnetic flux density, $|B_{new}|$ in Fig. 4(b). For this operation, a shape-preserving piecewise cubic interpolation is used. Though this method differs from other works [37, 38], the results are in good agreement with those obtained numerically using FEMM software.

3.4. Retaining Sleeve Winding and Eddy-Current Reaction Field

Eddy-current in conducting parts, such as RS or PM, has undesirable effects in rotating electrical machines, viz., producing heat and affecting the main magnetic field. If eddy-current reaction field is neglected, the induced currents and resulting losses can be calculated from magnetic field distribution and the derived electric field [63]. Surface charge density gradients generate gradients of electric field, and using square root scaled chart [64], it can be graphically evaluated for a conducting strip [65] and a bottleneck shaped sloppy conducting strip [66]. If reaction field is taken into consideration, the diffusion effect can be evaluated using MF method [40].

A conductive RS can behave as a shielding cylinder, decreasing eddy-current losses in the PM [41]. Thus, the derived quantities to evaluate induced current in this cylinder are referred using subscript *c*. Furthermore, the eddy-current reaction field also affects the produced torque, changing both net

torque and its oscillation [47]. The commonly adopted analytical model which considers such effect is complex [67] and relies on restricting assumptions, i.e., steady-state operation and under balanced three-phase condition [11, 39].

The analytical method adopted in this work was proposed by Polinder [68] and uses an auxiliary winding to account for the induced currents in the RS. Instead of solving the diffusion equation, RS currents are modeled as series of equivalent short-circuited sinusoidally-distributed windings, one each space harmonic. However, for the studied machine, the RS parameters allowed to disregard skin effect, which would be important only for frequencies above 18 kHz. This was justified from the skin-depth, δ_{skin}, as compared to RS width δ_c, that is $\delta_{skin} > \delta_c$. The skin-depth is given by

$$\delta_{skin} = \sqrt{\frac{\rho_c}{\pi \mu_0 \mu_r f}}, \tag{21}$$

where ρ_c is the RS resistivity, μ_r the RS relative permeability, and f the frequency. Therefore, the RS winding was defined as a surface current density at the mean radius r_c. This surface current density is accounted in the analytical model by dividing the RS region, as illustrated in Fig. 5.

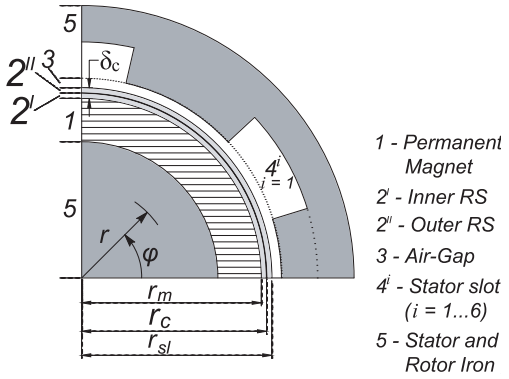

Figure 5. RS region redefinition to account for eddy-current.

For the two-dimensional analytical model, RS current only flows in the z-axis direction and is periodical in the circumferential direction. It is defined in the rotor reference frame by a Fourier series, that is

$$K_c(\varphi_r) = \sum_{k=1,3,5\ldots}^{\infty} \hat{K}_{c,k} \sin\left(k\left(\varphi_r - \gamma_k\right)\right), \tag{22}$$

where $\hat{K}_{c,k}$ is the k-th order of the winding density distribution with its magnetic axis along the angle γ_k. The surface current density is decomposed into two orthogonal sinusoidally distributed windings. This definition is useful for deriving voltage equations and equivalent circuit representing the RS. These orthogonal windings are expressed in the dq reference frame fixed in the rotor as

$$K_c(\varphi_r) = \sum_{k=1,3,5\ldots}^{\infty} \frac{N_{c,k}}{2r_c}\left(i_{cd\prime k} \sin(k\varphi_r) - i_{cq\prime k} \cos(k\varphi_r)\right), \tag{23}$$

where $N_{c,k}$ is effective number of turns of the k-th order winding. It can be chosen arbitrarily if the products $N_{c,k} i_{cd\prime k}$ and $N_{c,k} i_{cq\prime k}$ are kept constant [68]. Assuming negligible skin effect, the direct and quadrature axis currents, $i_{cd\prime k}$ and $i_{cq\prime k}$ respectively, are calculated by means of Faraday's and Ohm's law with the assumption that the current density is not a function of the radial position. From this, the surface current density is calculated as

$$K_c(\varphi_r) = -\frac{\delta_c}{\rho_c}\frac{\partial A_z}{\partial t}, \tag{24}$$

where ρ_c is the RS resistivity. A different approach to calculate the RS winding currents is using voltage equation of the short-circuited RS winding. Evaluating separately the contribution from different source

fields to the flux linkage, the direct and quadrature axis windings are written as

$$0 = R_{c,k} i_{cd,k} + \frac{d\lambda_{cd,pm,k}}{dt} + \frac{d\lambda_{cd,s,k}}{dt} + \frac{d\lambda_{cd,k}}{dt} \tag{25}$$

and

$$0 = R_{c,k} i_{dq,k} + \frac{d\lambda_{cq,pm,k}}{dt} + \frac{d\lambda_{cq,s,k}}{dt} + \frac{d\lambda_{cq,k}}{dt}, \tag{26}$$

where $\lambda_{cd,pm,k}$ is the k-th space harmonic flux linkage of the RS d-axis winding caused by magnets, $\lambda_{cd,s,k}$ the flux linkage due to the stator currents, and $\lambda_{cd,k}$ the flux linkage due to the RS d-axis winding current. Same reasoning applies to the RS q-axis winding, with $\lambda_{cq,pm,k}$, $\lambda_{cq,s,k}$, and $\lambda_{cq,k}$ being the contributions from magnet, stator current, and RS q-axis winding current, respectively. The resistance of the k-th space harmonic of the equivalent RS winding, $R_{c,k}$, is derived from Eqs. (23), (24), (25), and (26) [53], that is

$$R_{c,k} = \frac{\pi l_s \rho_c N_{c,k}^2}{4\delta_c r_c}, \tag{27}$$

where l_s is the machine axial length.

The dynamic equation is solved using numerical integration methods, such as Runge-Kutta method. Thus, the RS winding equations are rewritten in the form $i_c' = f(i_c, t)$, which requires the RS winding self-inductance definition. However, accounting for the space varying permeability produces a time varying self-inductance. As a result, Eqs. (25) and (26) are written as

$$\frac{di_{cd,k}}{dt} = -\frac{1}{L_{cd,k}} \left(R_{c,k} + \frac{dL_{cd,k}}{dt} \right) i_{cd,k} - \frac{1}{L_{cd,k}} \left(\frac{d\lambda_{cd,pm,k}}{dt} + \frac{d\lambda_{cd,s,k}}{dt} \right) \tag{28}$$

and

$$\frac{di_{cq,k}}{dt} = -\frac{1}{L_{cq,k}} \left(R_{c,k} + \frac{dL_{cq,k}}{dt} \right) i_{cq,k} - \frac{1}{L_{cq,k}} \left(\frac{d\lambda_{cq,pm,k}}{dt} + \frac{d\lambda_{cq,s,k}}{dt} \right). \tag{29}$$

The self-inductances are calculated at every time-step and at every iteration for the evaluation of nonlinear relative permeability by setting RS winding currents with unitary current. However, since inductances are calculated in the stator reference frame, and the dynamic equation is solved in the rotor reference frame, proper coordinate transformation must be carried out.

The novel method proposed in this work to account for skin effect is based on the RS winding method. The parameters used to define the surface current density, radius r_c, and width δ_c are reevaluated to account for the nonuniform distribution of alternating currents in the conducting region. As illustrated in Fig. 6, these parameters are defined according to the skin-depth, that is

$$\delta_c = \delta_{skin} = \sqrt{\frac{\rho_c}{\pi \mu_0 \mu_r f}} \tag{30}$$

and

$$r_c = r_{sl} - \frac{\delta_{skin}}{2}. \tag{31}$$

where for the purpose of evaluating Eq. (30), μ_r is the unsaturated RS relative permeability.

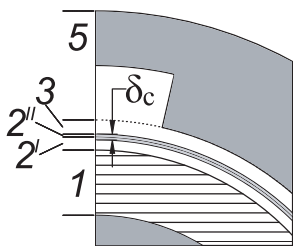

Figure 6. RS winding redefinition for evaluation of skin-effect.

The RS winding method can also be adopted to account for the space-varying permeability. In this manner, the circumferential boundary condition on the interface between the inner and outer RSs, which is used to define the surface current density. The RS winding parameters, defined in Eqs. (30) and (31), are derived using the unsaturated RS permeability to keep boundary at constant radius, as required by the adopted MF method. Using the same reasoning as discussed in Section 3, that is

$$\frac{B_{\varphi}^{(2^I)}(r_c,\varphi_s)}{\mu_r(\varphi_s)\mu_0} - \frac{B_{\varphi}^{(2^{II})}(r_c,\varphi_s)}{\mu_r(\varphi_s)\mu_0} = -K_c(\varphi_s). \tag{32}$$

The boundary condition is solved using the relations in Tables 2 and 3, that is

$$\begin{aligned}\hat{B}_{(s)\varphi,k}^{(2^I)}(r_c) - \hat{B}_{(s)\varphi,k}^{(2^{II})}(r_c) \;=\; -\sum_{m=0,1,2,3,\ldots}^{\infty}\Bigg[&\frac{\hat{\mu}_{(c)r,m}\mu_0}{2}\left(\hat{K}_{(s)cdq,k-2m}+\hat{K}_{(s)cdq,k+2m}-\hat{K}_{(s)cdq,2m-k}\right)\\ &+\frac{\hat{\mu}_{(s)r,m}\mu_0}{2}\left(\hat{K}_{(c)cdq,k-2m}-\hat{K}_{(c)cdq,k+2m}+\hat{K}_{(c)cdq,2m-k}\right)\Bigg]\end{aligned} \tag{33}$$

and

$$\begin{aligned}\hat{B}_{(c)\varphi,k}^{(2^I)}(r_c) - \hat{B}_{(c)\varphi,k}^{(2^{II})}(r_c) \;=\; -\sum_{m=0,1,2,3,\ldots}^{\infty}\Bigg[&\frac{\hat{\mu}_{(c)r,m}\mu_0}{2}\left(\hat{K}_{(c)cdq,k-2m}+\hat{K}_{(c)cdq,k+2m}+\hat{K}_{(c)cdq,2m-k}\right)\\ &+\frac{\hat{\mu}_{(s)r,m}\mu_0}{2}\left(-\hat{K}_{(s)cdq,k-2m}+\hat{K}_{(s)cdq,k+2m}+\hat{K}_{(s)cdq,2m-k}\right)\Bigg]\end{aligned} \tag{34}$$

where $\hat{K}_{(c)cdq,k}$ is the k-th order cosine Fourier coefficient of the direct-axis or quadrature-axis winding. In the present work, these are calculated separately for the eddy-currents evaluation, which require individual self-inductance calculation as defined in Eqs. (28) and (29). Also, Eq. (32) is written in the stator reference frame, thus requiring a coordinate transformation of the calculated surface density.

The partitioning of RS region into two regions demands the reassessment of variable relative permeability methodology. As the flux density is calculated differently within each region, the proposed method evaluates three different space-varying permeabilities, one at the mean radius of region $2^I, r_{c1}$, one the mean radius of region $2^{II}, r_{c2}$, and a third in the boundary, r_c. The iterative method, as discussed in Subsection 3.3, is applied to each of these three relative permeabilities, and the convergence condition is established from the maximum of the calculated errors using MAPE method.

4. RESULTS AND VALIDATION

The objective of this section is to validate the proposed method, evaluating the model assumptions according to magnetic characteristics deviation observed in a high-speed generator prototype, as detailed in Section 2. The results for the two-dimensional semi-analytical method are compared with those from FEMM software [14]. The geometrical parameters and material properties are derived from the HS surface-mounted PM machine, as given in Table 4.

The RS relative permeability presents a nonlinear characteristic and is modeled in this work accordingly. The stator currents are defined as three-phase sinusoidal and balanced system with a phase angle defined to produce a resultant magnetic flux which is orthogonal to the PM magnetic flux.

First, the proposed method to account for the space-varying relative permeability is evaluated, along with the iterative method effectiveness to solve the material non-linearity. For the simulation, the rotor angular position is kept constant, and the eddy-current reaction field is disregarded. The results for the relative permeability, evaluated at the RS mean radius, considering two rotor positions and for two loading conditions, are illustrated in Fig. 7.

The analysis of the proposed method to account for eddy-current reaction field is first carried out with a constant and homogeneous RS relative permeability, i.e., $\mu_r = 300$. However, a limitation is presented by the FEMM software, in which the time-harmonic magnetic problem is solved for one fixed frequency. Thus, for harmonic problems, the PM magnetic field is disregarded as it is time independent. For the sake of assessing the proposed method, the problem formulation was simplified.

Table 4. Parameters for analytical model of the slotted geometry.

Parameters	Symbol	Value
Number of turns per coil	N_s	16
Radius of rotor yoke	r_{rl}	7.5 mm
Radius of magnet surface	r_m	9.8935 mm
Radius of retaining sleeve surface	r_{sl}	10.475 mm
Radius of stator inner surface	r_s	11.0 mm
Radius of stator slot outer surface	r_{sa}	15.0 mm
Stator axial length	l_s	100.0 mm
Number of phases	m	3
Number of pole-pairs	p	1
Number of slots	Q_s	6
Slot-opening angle	b_{sa}	10.4316°
PM remanent magnetization	B_{rem}	1.08 T
PM magnetization distribution		parallel
PM relative recoil permeability	μ_{rec}	1.049
RS resistivity	ρ_c	$6.9 \times 10^{-7}\,\Omega$m
RS unsaturated relative permeability	μ_r	300

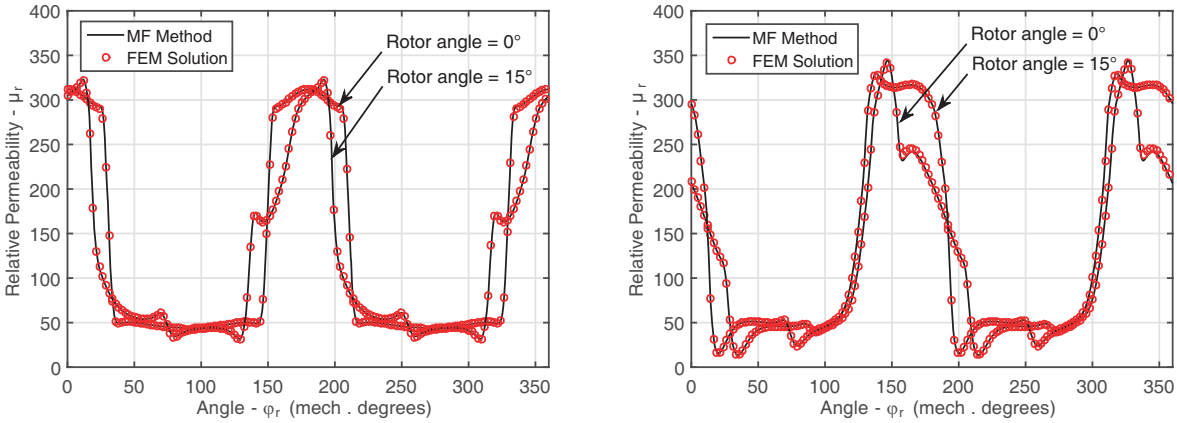

Figure 7. Space-varying relative permeability solution for two rotor positions, 0° and 15°, and two operating conditions: (a) no-load condition; and (b) armature reaction field considered with $|I_s| = 15\ A_{peak}$.

The rotor angular position is kept constant, and the stator currents are defined sinusoidal and balanced. The results for three different electrical frequencies are illustrated in Fig. 8. In all cases, stator loading is considered with peak phase current of $|I_s| = 10\ A_{peak}$. For comparison, the result disregarding the diffusion effect, i.e., $\rho_c \to \infty$, is presented.

The evaluated frequencies are chosen to test the validity of the proposed methodology. For the machine operating at rated speed, 70 krpm, the fundamental frequency of 1.17 kHz would permit neglecting skin effect, with skin-depth greater than RS width. The slotting effect influences the induced RS currents frequency, f_c, where the pulsation of magnetic flux density, from either PM or stator currents, is related to the number of slots, that is $f_c = n6 \cdot f_1,\ n = [1, 2, 3, \ldots]$ for the studied machine

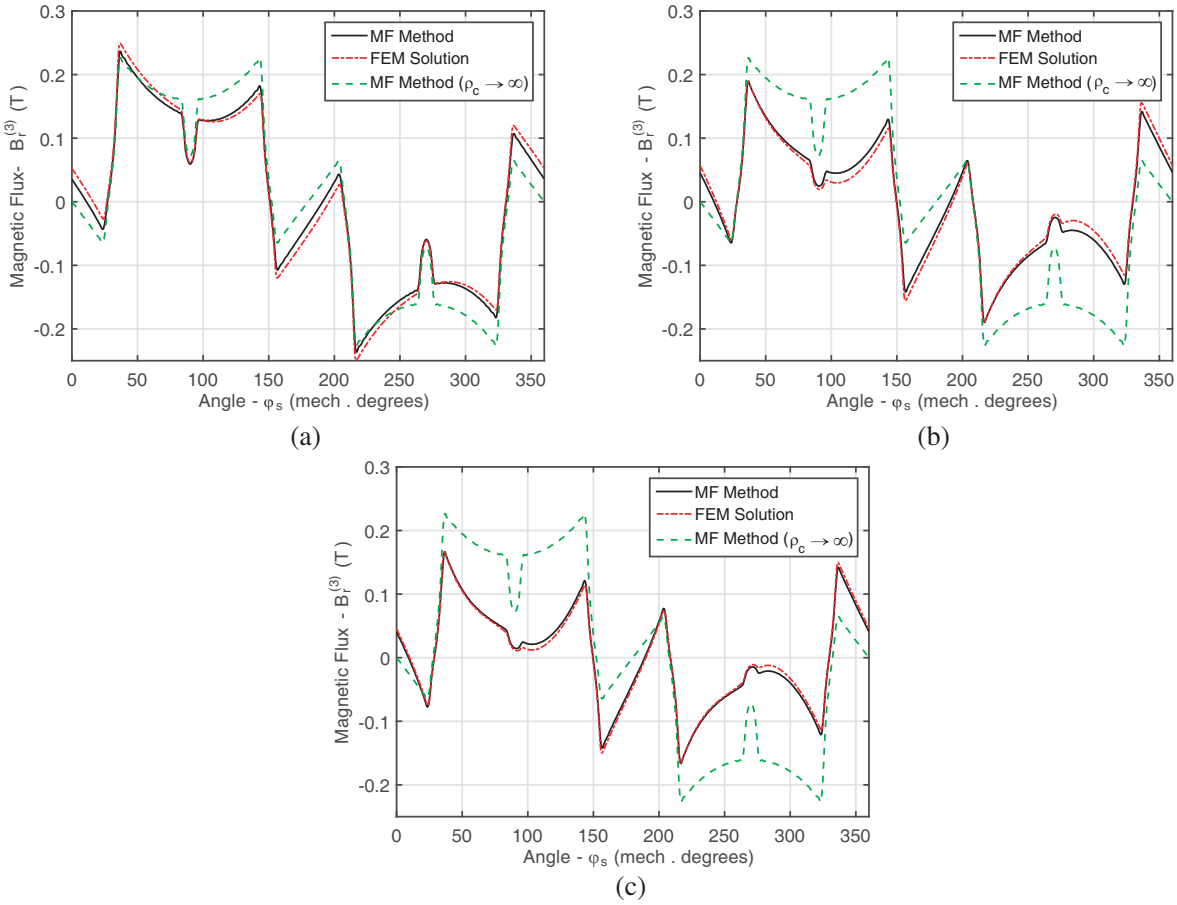

Figure 8. Analytical and numerical simulation for eddy-current reaction field and homogeneous RS permeability: (a) $f = 1.17$ kHz; (b) $f = 7$ kHz; and (c) $f = 14$ kHz.

[68]. Though the proposed methodology limits the skin-effect correction to one frequency, Eqs. (30) and (31), the induced current fundamental frequency has a pronounced value over the harmonics. Therefore, for the stator current frequency of 7 kHz, results are in good agreement with those from FEM. The twelfth time harmonic, that is 14 kHz, is also studied to evaluate higher frequency content, where MF method also provided result in agreement with numerical solution.

The improved method is evaluated in similar conditions previously considered, but accounting for nonlinear RS relative permeability and eddy-current reaction fields. The results obtained from MF method and FEM are presented in Fig. 9 for the same frequencies and same loading condition.

For the described assumptions, the proposed method presents better results for eddy-current reaction field as frequency is increased. In comparison with eddy-current reaction field analysis using Helmholtz equation, which provides formal solution to the diffusion effect, the proposed method assumptions are more limiting. The RS equivalent winding parameter corrections are carried out in terms of one frequency, where the induced currents have non-sinusoidal waveform. The current distribution along the RS would greatly affect the saturation profile, which is not fully evaluated by a surface current density, as defined. However, it can overcome some of the conventional method limitations, such as dynamic study of electrical machines at unbalanced condition. These advantages, along with the proper evaluation of machine parameters, can extend MF method application to control and fault analysis.

Finally, the improved method is used to investigate the adopted model assumptions on the machine electromagnetic performance. A comparative study is carried out to illustrate the effect of the non-homogeneous permeability and diffusion effect on the no-load induced voltage, or back-EMF, and the

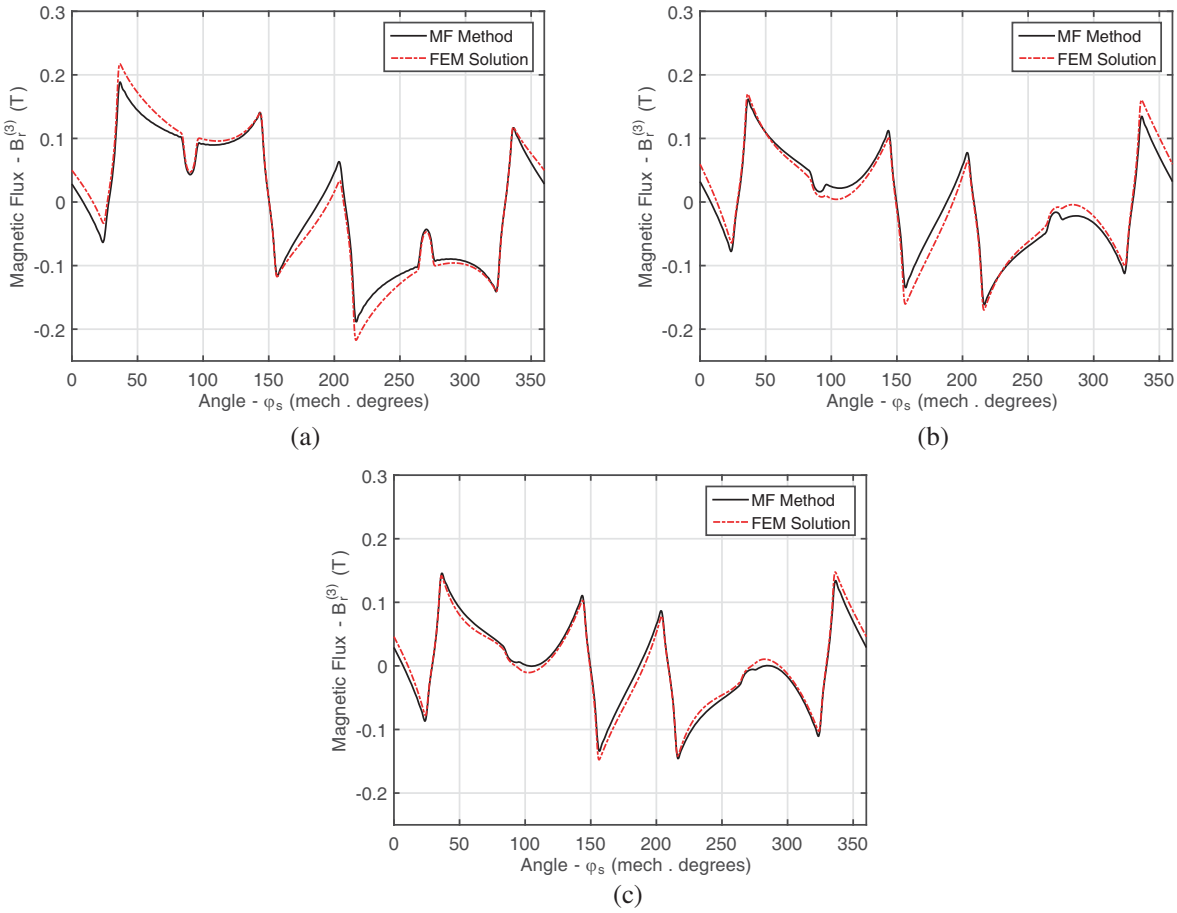

Figure 9. Analytical and numerical simulation for eddy-current reaction field and non-homogeneous RS permeability: (a) $f = 1.17\,\text{kHz}$; (b) $f = 7\,\text{kHz}$; and (c) $f = 14\,\text{kHz}$.

on-load produced torque with $|I_s| = 10\ A_{peak}$. First, the analytical calculation of the back-EMF for the slotted structure uses the method based on Stokes theorem, evaluating the magnetic vector potential in the stator slots [35, 36]. The electromagnetic torque is computed using the Maxwell stress tensor [21, 25].

For the comparative study, the PM generator retaining sleeve is analyzed with homogeneous permeability, which is considered both the ideal non-magnetic and increased permeabilities, with $\mu_r = 1$ and $\mu_r = 300$, respectively. Furthermore, the machine is evaluated with space-varying relative permeability, with and without diffusion effect. In this study, the proposed method taking the diffusion effect into consideration is not compared with FEM result, as the FEMM software does not provide the required time-dependent modeling. For the remainder evaluated conditions, the results are in agreement with those from FEM, as illustrated in Fig. 10 for the back-EMF and in Fig. 11 for the electromagnetic torque.

The result provides interesting insight into the permeable retaining sleeve proposal. Considering only an increased homogeneous relative permeability, the pole-to-pole flux leakage significantly reduces the produced torque and back-EMF, as can be seen from Fig. 11(d) and Fig. 10(d). However, the nonlinear characteristic of the RS material reduces this leakage effect and establishes a preferable magnetic path. With the increased relative permeability in the main magnetic circuit, the net torque and induced voltage are increased, as illustrated in Fig. 11(b) and Fig. 10(b). However, this comes with cost, as the torque oscillation grows, reaching 4.5% of the net torque. This oscillating torque is problematic in HS machines, especially those operating above its first natural frequency [55]. The conducting RS changed the oscillating torque profile, but the reduction in net torque is more pronounced. Similar result is discussed in [69].

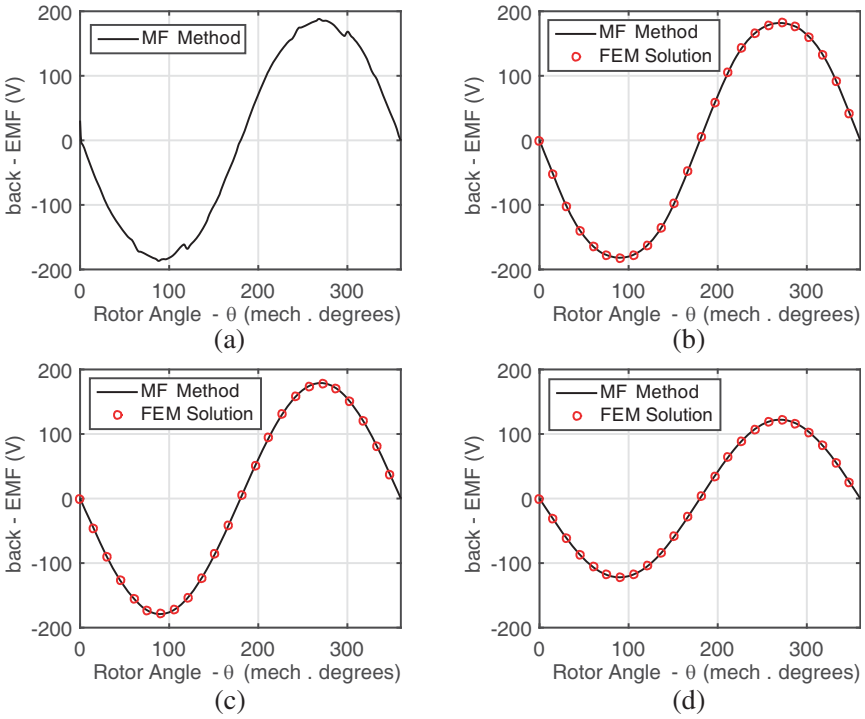

Figure 10. Back-EMF for different RS material model assumptions: (a) space-varying permeability and conductive; (b) space-varying permeability and non-conductive; (c) linear permeability with $\mu_r = 1$; and (d) linear permeability with $\mu_r = 300$.

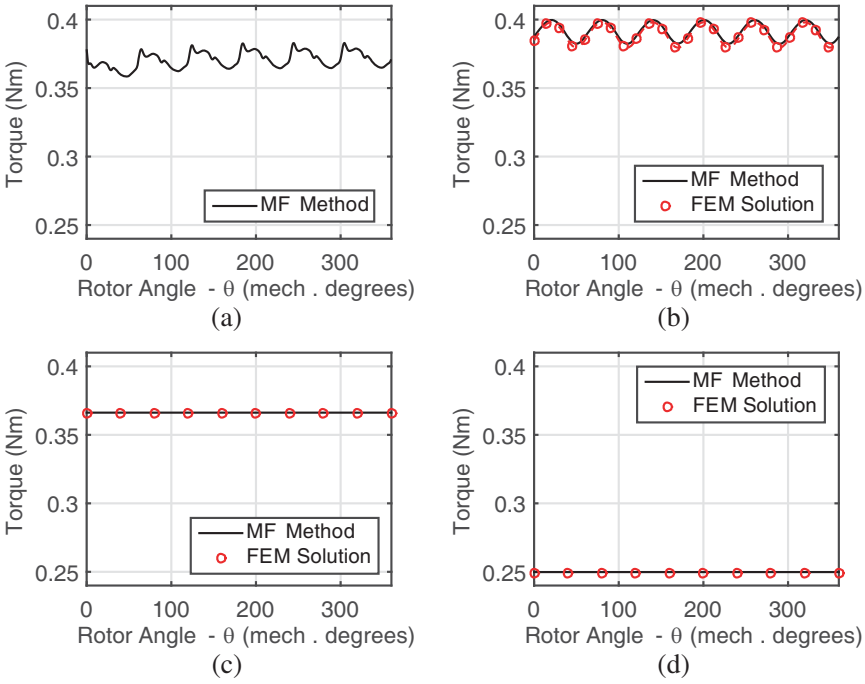

Figure 11. Electromagnetic torque for different RS parameter model assumptions: (a) space-varying permeability and conductive; (b) space-varying permeability and non-conductive; (c) linear permeability with $\mu_r = 1$; and (d) linear permeability with $\mu_r = 300$.

5. CONCLUSIONS

In this work, the Maxwell-Fourier method is improved for calculating magnetic field in high-speed surface-mounted PM machine with permeable retaining sleeve. The developed model incorporates the saturation phenomenon of the non-homogeneous region through a space-varying relative permeability. With the assumption that saturation affects the relative permeability along the circumferential length of the region, a Fourier series is used to express this relation, and its coefficients are calculated according to the machine operation condition using iterative method.

The retaining sleeve is composed of conducting material, and the induced currents reaction is known to affect machine performance. This behavior is contemplated with the use of a surface current density within the sleeve region, defined as a series of equivalent short-circuited sinusoidally-distributed windings. The model is suitable for the proposed nonhomogeneous permeability formulation and considers skin effect, which accounts for by revising the auxiliary winding parameters.

The novel MF method results show good agreement with those obtained from finite-element method. The RS space-varying permeability, calculated through iterative method, presents a similar saturation profile as the results from FEM. For the conducting RS, eddy-current reaction field, including skin effect, is evaluated for homogeneous and nonhomogeneous RS permeability. HS machine electromagnetic performance, viz., the back-EMF and torque, is evaluated with different model assumptions, showing the importance of the correct model definition.

Being derived from well-established Maxwell-Fourier formulation, it can be applied to other machine topologies and is suitable for use with other MF method researched improvements. For instance, this work evaluates slotting effect with subdomain method. The proposed method advantages can help overcome Maxwell-Fourier method limitations, such as the need to define linear material parameter, evaluation of machine in steady-state operation and under balanced condition.

ACKNOWLEDGMENT

This study was financed in part by the Coordenação de Aperfeiçoamento de Pessoal de Nível Superior — Brasil (CAPES) — Finance Code 001, the Conselho Nacional de Desenvolvimento Científico e Tecnológico (CNPq) and the Universidade Federal de Minas Gerais (UFMG).

REFERENCES

1. Uzhegov, N., E. Kurvinen, J. Nerg, J. Pyrhonen, J. T. Sopanen, and S. Shirinskii, "Multidisciplinary design process of a 6-slot 2-pole high-speed permanent-magnet synchronous machine," *IEEE Transactions on Industrial Electronics*, Vol. 63, No. 2, 784–795, Feb. 2016.
2. Shen, J., X. Qin, and Y. Wang, "High-speed permanent magnet electrical machines — Applications, key issues and challenges," *CES Transactions on Electrical Machines and Systems*, Vol. 2, No. 1, 23–33, Mar. 2018.
3. Lahne, H.-C. and D. Gerling, "Comparison of state-of-the-art high-speed high-power machines: Research study including a design example of a 50000 rpm induction machine," *IECON 2015 — 41st Annual Conference of the IEEE Industrial Electronics Society*, 003519–003524, IEEE, Nov. 2015.
4. Tenconi, A., S. Vaschetto, and A. Vigliani, "Electrical machines for high-speed applications: Design considerations and tradeoffs," *IEEE Transactions on Industrial Electronics*, Vol. 61, No. 6, 3022–3029, Jun. 2014.
5. Cupertino, F., R. Leuzzi, V. G. Monopoli, and G. L. Cascella, "Design procedure for high-speed PM motors aided by optimization algorithms," *Machines*, Vol. 6, No. 1, 5, Feb. 2018.
6. Uzhegov, N., J. Barta, J. Kurfurst, C. Ondrusek, and J. Pyrhonen, "Comparison of high-speed electrical motors for a turbo circulator application," *IEEE Transactions on Industry Applications*, Vol. 53, No. 5, 4308–4317, Sep. 2017.
7. Gerada, D., D. Borg-Bartolo, A. Mebarki, C. Micallef, N. L. Brown, and C. Gerada, "Electrical machines for high speed applications with a wide constant-power region requirement," *2011 International Conference on Electrical Machines and Systems*, 1–6, Aug. 2011.

8. Gilson, A., F. Dubas, D. Depernet, and C. Espanet, "Comparison of high-speed pm machine topologies for electrically-assisted turbocharger applications," *2016 19th International Conference on Electrical Machines and Systems (ICEMS)*, 1–5, 2016.
9. Gerada, D., A. Mebarki, N. L. Brown, C. Gerada, A. Cavagnino, and A. Boglietti, "High-speed electrical machines: Technologies, trends, and developments," *IEEE Transactions on Industrial Electronics*, Vol. 61, No. 6, 2946–2959, Jun. 2014.
10. Pottie, D. L., G. A. Mendonça, O. A. Faria, M. T. C. Faria, B. J. Cardoso Filho, and T. A. Maia, "Some aspects of the electromechanical design of high-speed microturbines for power generation," *International Journal of Applied Electromagnetics and Mechanics*, Vol. 63, No. 4, 621–644, Aug. 2020.
11. Hannon, B., P. Sergeant, L. Dupre, and P.-D. Pfister, "Two-dimensional fourier-based modeling of electric machines — An overview," *IEEE Transactions on Magnetics*, Vol. 55, No. 10, 1–17, Oct. 2019.
12. Gieras, J. F., *Permanent Magnet Motor Technology*, 3rd edition, Taylor & Francis Inc., 2009.
13. Pyrhonen, V. H. and T. Jokinen, *Design Rotating Electrical Machines*, John Wiley & Sons, 2013.
14. Meeker, D., *Finite Element Method Magnetics*, v4.2, 2015.
15. Pfister, P.-D., X. Yin, and Y. Fang, "Slotted permanent-magnet machines: General analytical model of magnetic fields, torque, eddy currents, and permanent-magnet power losses including the diffusion effect," *IEEE Transactions on Magnetics*, Vol. 52, No. 5, 1–13, May 2016.
16. Yu, Y., D. Liang, and X. Liu, "Optimal design of the rotor structure of a HSPMSM based on analytic calculation of eddy current losses," *Energies*, Vol. 10, No. 4, 551, Apr. 2017.
17. Mohamed, M. R. and D. Ishak, "Optimization of surface-mounted permanent magnet brushless AC motor using analytical model and differential evolution algorithm," *Journal of Electrical Engineering*, Vol. 70, No. 3, 208–217, Jun. 2019.
18. Jumayev, S., K. O. Boynov, J. J. H. Paulides, E. A. Lomonova, and J. Pyrhonen, "Slotless PM machines with skewed winding shapes: 3-D electromagnetic semianalytical model," *IEEE Transactions on Magnetics*, Vol. 52, No. 11, 1–12, Nov. 2016.
19. Tiegna, H., Y. Amara, and G. Barakat, "Overview of analytical models of permanent magnet electrical machines for analysis and design purposes," *Mathematics and Computers in Simulation*, Vol. 90, 162–177, Apr. 2013.
20. Dubas, F. and K. Boughrara, "New scientific contribution on the 2-D subdomain technique in cartesian coordinates: Taking into account of iron parts," *Mathematical and Computational Applications*, Vol. 22, No. 1, 17, Feb. 2017.
21. Rahideh, A., H. Moayed-Jahromi, M. Mardaneh, F. Dubas, and T. Korakianitis, "Analytical calculations of electromagnetic quantities for slotted brushless machines with surface-inset magnets," *Progress In Electromagnetics Research B*, Vol. 72, 49–65, 2017.
22. Yu, Y., Q. W. Xiang, X. Zhang, and W. Zhang, "Analytical model of the magnetic field distribution of a generator combined with magnetic bearing in wind turbines," *Progress In Electromagnetics Research B*, Vol. 81, 25–44, 2018.
23. Benmessaoud, Y., D. Ouamara, F. Dubas, and M. Hilairet, "Investigation of volumic permanent-magnet eddy-current losses in multi-phase synchronous machines from hybrid multi-layer model," *Mathematical and Computational Applications*, Vol. 25, No. 1, 14, Mar. 2020.
24. Oner, Y., Z. Q. Zhu, L. J. Wu, X. Ge, H. Zhan, and J. T. Chen, "Analytical on-load subdomain field model of permanent-magnet vernier machines," *IEEE Transactions on Industrial Electronics*, Vol. 63, No. 7, 4105–4117, Jul. 2016.
25. Lubin, T., S. Mezani, and A. Rezzoug, "Improved analytical model for surface-mounted PM motors considering slotting effects and armature reaction," *Progress In Electromagnetics Research B*, Vol. 25, 293–314, 2010.
26. Zhu, Z., D. Howe, and C. Chan, "Improved analytical model for predicting the magnetic field distribution in brushless permanent-magnet machines," *IEEE Transactions on Magnetics*, Vol. 38, No. 1, 229–238, 2002.

27. Ackermann, B. and R. Sottek, "Analytical modeling of the cogging torque in permanent magnet motors," *Electrical Engineering*, Vol. 78, No. 2, 117–125, Mar. 1995.
28. Roubache, L., K. Boughrara, F. Dubas, and R. Ibtiouen, "Semi-analytical modeling of spoke-type permanent-magnet machines considering the iron core relative permeability: Subdomain technique and taylor polynomial," *Progress In Electromagnetics Research B*, Vol. 77, 85–101, 2017.
29. Faiz, J., M. Hassanzadeh, and A. Kiyoumarsi, "Analytical calculation of magnetic field in surfacemounted permanent-magnet machines with air-gap eccentricity," *COMPEL — The International Journal for Computation and Mathematics in Electrical and Electronic Engineering*, Vol. 38, No. 2, 893–914, Mar. 2019.
30. Djelloul-Khedda, Z., K. Boughrara, F. Dubas, A. Kechroud, and A. Tikellaline, "Analytical prediction of iron-core losses in flux-modulated permanent-magnet synchronous machines," *IEEE Transactions on Magnetics*, Vol. 55, No. 1, 1–12, Jan. 2019.
31. Boughrara, K., T. Lubin, and R. Ibtiouen, "General subdomain model for predicting magnetic field in internal and external rotor multiphase flux-switching machines topologies," *IEEE Transactions on Magnetics*, Vol. 49, No. 10, 5310–5325, Oct. 2013.
32. Devillers, E., J. L. Besnerais, T. Lubin, M. Hecquet, and J.-P. Lecointe, "A review of subdomain modeling techniques in electrical machines: Performances and applications," *2016 XXII International Conference on Electrical Machines (ICEM)*, 86–92, IEEE, Sep. 2016.
33. Ortega, A. J. P., "Fast design of asymmetrical permanent magnet synchronous machines that minimize pulsating torque," *Progress In Electromagnetics Research B*, Vol. 76, 111–123, 2017.
34. Alam, F. R. and K. Abbaszadeh, "Magnetic field analysis in eccentric surface-mounted permanentmagnet motors using an improved conformal mapping method," *IEEE Transactions on Energy Conversion*, Vol. 31, No. 1, 333–344, Mar. 2016.
35. Boughrara, K., T. Lubin, R. Ibtiouen, and N. Benallal, "Analytical calculation of parallel double excitation and spoke-type permanent-magnet motors; simplified versus exact model," *Progress In Electromagnetics Research B*, Vol. 47, 145–178, 2013.
36. Brahim, L.-C., K. Boughrara, and R. Ibtiouen, "Cogging torque minimization of surface-mounted permanent magnet synchronous machines using hybrid magnet shapes," *Progress In Electromagnetics Research B*, Vol. 62, 49–61, 2015.
37. Djelloul-Khedda, Z., K. Boughrara, F. Dubas, and R. Ibtiouen, "Nonlinear analytical prediction of magnetic field and electromagnetic performances in switched reluctance machines," *IEEE Transactions on Magnetics*, Vol. 53, No. 7, 1–11, Jul. 2017.
38. Roubache, L., K. Boughrara, F. Dubas, and R. Ibtiouen, "Elementary subdomain technique for magnetic field calculation in rotating electrical machines with local saturation effect," *COMPEL — The International Journal for Computation and Mathematics in Electrical and Electronic Engineering*, Vol. 38, No. 1, 24–45, Jan. 2019.
39. Holm, S. R., H. Polinder, and J. A. Ferreira, "Analytical modeling of a permanent-magnet synchronous machine in a ywheel," *IEEE Transactions on Magnetics*, Vol. 43, No. 5, 1955–1967, May 2007.
40. Ouamara, D. and F. Dubas, "Permanent-magnet eddy-current losses: A global revision of calculation and analysis," *Mathematical and Computational Applications*, Vol. 24, No. 3, 67, Jul. 2019.
41. Boubaker, N., D. Matt, P. Enrici, F. Nierlich, G. Durand, F. Orlandini, X. Longère, and J. Aïgba, "Study of eddy-current loss in the sleeves and Sm-Co magnets of a high-performance SMPM synchronous machine (10 kRPM, 60 kW)," *Electric Power Systems Research*, Vol. 142, 20–28, Jan. 2017.
42. Zhu, Z., K. Ng, N. Schofield, and D. Howe, "Analytical prediction of rotor eddy current loss in brushless machines equipped with surface-mounted permanent magnets. I. Magnetostatic field model," *ICEMS'2001. Proceedings of the Fifth International Conference on Electrical Machines and Systems (IEEE Cat. No.01EX501)*, Int. Acad. Publishers, 2001.
43. Zhou, F., J. Shen, W. Fei, and R. Lin, "Study of retaining sleeve and conductive shield and their in fluence on rotor loss in high-speed PM BLDC motors," *IEEE Transactions on Magnetics*, Vol. 42,

No. 10, 3398–3400, Oct. 2006.

44. Zhang, C., L. Chen, S. Yu, X. Ma, X. Wang, and R. Tang, "Performance characteristics of high speed permanent magnet machine with different rotor retaining sleeve," *2019 22nd International Conference on Electrical Machines and Systems (ICEMS)*, IEEE, Aug. 2019.
45. Qiu, H., Q. Duan, L. Yao, Y. Dong, R. Yi, G. Cui, and W. Li, "Analytical analysis of sleeve permeability for output performance of high speed permanent magnet generators driven by micro gas turbines," *Applied Mathematical Modelling*, Vol. 40, No. 21-22, 9017–9028, Nov. 2016.
46. Patel. A. N. and A. Kapil, "Effect of magnet retaining sleeve thickness on cogging torque of radial flux permanent magnet brushless DC motor," *2016 International Conference on Emerging Trends in Engineering, Technology and Science (ICETETS)*, 1–3, IEEE, Feb. 2016.
47. Hannon, B., P. Sergeant, and L. Dupre, "Evaluation of the torque in high-speed PMSMs with a shielding cylinder and BLDC control," *IEEE Transactions on Magnetics*, Vol. 54, No. 10, 1–8, Oct. 2018.
48. Li, W., H. Qiu, X. Zhang, J. Cao, and R. Yi, "Analyses on electromagnetic and temperature fields of superhigh-speed permanent-magnet generator with different sleeve materials," *IEEE Transactions on Industrial Electronics*, Vol. 61, No. 6, 3056–3063, Jun. 2014.
49. Zhu, Z., Y. Huang, J. Dong, F. Peng, and Y. Yao, "Rotor eddy current loss reduction with permeable retaining sleeve for permanent magnet synchronous machine," *IEEE Transactions on Energy Conversion*, 1–1, 2020.
50. Yon, J. M., P. H. Mellor, R. Wrobel, J. D. Booker, and S. G. Burrow, "Analysis of semipermeable containment sleeve technology for high-speed permanent magnet machines," *IEEE Transactions on Energy Conversion*, Vol. 27, No. 3, 646–653, Sep. 2012.
51. Mendonça, G., T. Maia, and B. C. Filho, "Magnetic field analytical solution for non-homogeneous permeability in retaining sleeve of a high-speed permanent-magnet machine," *Mathematical and Computational Applications*, Vol. 23, No. 4, 72, Nov. 2018.
52. Ramakrishnan, K., M. Curti, D. Zarko, G. Mastinu, J. J. H. Paulides, and E. A. Lomonova, "Comparative analysis of various methods for modelling surface permanent magnet machines," *IET Electric Power Applications*, Vol. 11, No. 4, 540–547, Apr. 2017.
53. Polinder, H. and M. J. Hoeijmakers, "Modelling a PM machine with shielding cylinder," *9th International Conference on Electrical Machines and Drives*, 16–20, IEE, 1999.
54. Maia, T. A., J. E. Barros, B. J. C. Filho, and M. P. Porto, "Experimental performance of a low cost micro-CAES generation system," *Applied Energy*, Vol. 182, 358–364, Nov. 2016.
55. Maia, T. A., O. A. Faria, J. E. Barros, M. P. Porto, and B. J. C. Filho, "Test and simulation of an electric generator driven by a micro-turbine," *Electric Power Systems Research*, Vol. 147, 224–232, Jun. 2017.
56. Dutta, R., K. Ahsanullah, and F. Rahman, "Cogging torque and torque ripple in a direct-drive interior permanent magnet generator," *Progress In Electromagnetics Research B*, Vol. 70, 73–85, 2016.
57. Boyce, W., *Elementary Differential Equations and Boundary Value Problems*, Wiley, Hoboken, NJ, 2005.
58. Dubas, F. and C. Espanet, "Analytical solution of the magnetic field in permanent-magnet motors taking into account slotting effect: No-load vector potential and flux density calculation," *IEEE Transactions on Magnetics*, Vol. 45, No. 5, 2097–2109, May 2009.
59. Wu, L., Z. Zhu, D. Staton, M. Popescu, and D. Hawkins, "Analytical prediction of electromagnetic performance of surface-mounted PM machines based on subdomain model accounting for toothtips," *IET Electric Power Applications*, Vol. 5, No. 7, 597, 2011.
60. Tiang, T. L., D. Ishak, and M. K. M. Jamil, "Complete subdomain model for surface-mounted permanent magnet machines," *2014 IEEE Conference on Energy Conversion (CENCON)*, 140–145, IEEE, Oct. 2014.
61. Rahideh, A. and T. Korakianitis, "Analytical calculation of open-circuit magnetic field distribution of slotless brushless PM machines," *International Journal of Electrical Power & Energy Systems*,

Vol. 44, No. 1, 99–114, Jan. 2013.

62. Boutora, Y., N. Takorabet, and R. Ibtiouen, "Analytical model on real geometries of magnet bars of surface permanent magnet slotless machine," *Progress In Electromagnetics Research B*, Vol. 66, 31–47, 2016.
63. Jassal, A.. H. Polinder, and J. Ferreira, "Literature survey of eddy-current loss analysis in rotating electrical machines," *IET Electric Power Applications*, Vol. 6, No. 9, 743, 2012.
64. Gürdal, O., "A new approach to graphically reveal some unknown properties of theorthogonal coordinate systems in quadric form, by using the square root scaled chart," *Journal of the Faculty of Engineering and Architecture of Gazi University*, Vol. 23, No. 2, 317–327, 2008.
65. Gürdal, O., "Graphical exploration of the trajectories of electric fields and equipotentials outside the conducting strip carrying steady current," 2018, doi: 10.13140/RG.2.2.15757.79843.
66. Gürdal, O., "Graphical exploration of the trajectories of electric fields and equipotentials inside & outside infinitely long bottleneck shaped sloppy conducting strips carrying steady current," 2020, doi: 10.13140/RG.2.2.25959.19367.
67. Wu, L. J., Z. Q. Zhu, D. Staton, M. Popescu, and D. Hawkins, "Analytical model for predicting magnet loss of surface-mounted permanent magnet machines accounting for slotting effect and load," *IEEE Transactions on Magnetics*, Vol. 48, No. 1, 107–117, Jan. 2012.
68. Polinder, H., "On the losses in a high-speed permanent-magnet generator with rectifier," PhD Thesis, Delft University of Technology, 1998.
69. Hannon, B., P. Sergeant, and L. Dupre, "Two-dimensional fourier-based modeling of electric machines," *2017 IEEE International Electric Machines and Drives Conference (IEMDC)*, 1–8, IEEE, May 2017.